Stability of imploding shocks generated by underwater electrical explosion of cylindrical wire array

M. Kozlov, V. Tz. Gurovich, and Ya. E. Krasik
Physics Department, Technion, Haifa 32000, Israel

(Received 20 June 2013; accepted 14 October 2013; published online 1 November 2013)

The results of two-dimensional hydrodynamic simulations of the dynamics and stability of azimuthal non-uniformities in converging shock waves generated by an underwater explosion of a cylindrical wire array and their effect on the cumulation of energy in the vicinity of the converging axis are presented. It has been shown that in spite of the fact that such non-uniformities are always weakly unstable, for a broad range of experimentally relevant regimes these non-uniformities remain small and do not significantly affect the cumulation of energy. Only the non-uniformities with wavelengths comparable to the distance from the axis of convergence exhibit substantial growth that considerably attenuates the energy cumulation. © *2013 AIP Publishing LLC*.
[http://dx.doi.org/10.1063/1.4827262]

I. INTRODUCTION

The generation of extreme states of matter by converging shock waves (SWs) has been the subject of intense study due to their importance for hydrodynamics, space and plasma physics,[1] and their potential application for the ignition of inertial confinement fusion. Several methods of generating converging SWs, including laser irradiation of a target,[2] the Z-pinch approach,[3] underwater chemical,[4] electrical explosions of cylindrical or spherical wire arrays,[5] and high-velocity impact with conical targets initiated by chemical explosions,[6] have been studied in the context of inertial confinement fusion.

In general, the energy density cumulation due to the cylindrical (spherical) symmetry depends crucially on the stability of the converging SW front. Different types of instabilities have been thoroughly studied in SW propagating in gases and plasmas.[7–15] There is a general understanding that in plasmas the energy accumulated by a cylindrically or spherically converging SW is significantly diminished by instabilities in the SW front (see for example Ref. 7). The unstable growth of converging SW front perturbations resulting from Raleigh-Taylor instability hinders the realization of laser-confinement fusion,[16] while the development of sausage and kink modes due to magneto-hydrodynamic instabilities has been a major obstacle in the Z-pinch approach.[17] In the case of high-velocity impact with conical targets,[6] the perturbations of the interface between the heavy target material and light fuel exhibit unstable growth because of the Richtmyer–Meshkov instability at the initial stages of impact,[18] but this instability decays as the shock wave proceeds to the axis of symmetry resulting in a rather smooth interface at that location. In general, in spite of the prolonged research of converging SW stability, there is no complete answer about the range of applicability and, respectively, the correctness of solutions for the limit of cumulations of cylindrical and spherical SWs.[10,11] For instance, in a review by Sokolov[7] of different instabilities of converging SW, one can find models that show that, in the case of water, the converging SW is stable even in linear approximation and small perturbations cannot limit cumulations.

Recent experiments on underwater electrical wire explosion (UEWE) showed that this approach can be used to generate strong SW efficiently due to the several important advantages that it has as compared with electrical wire explosion in vacuum. These advantages are the absence of a shunting plasma shell, which could intercept a significant part of the discharge current, relatively high efficiency ($\sim$12%) of the transfer of the deposited energy from the exploding wires to the converging water flow, and low decay of the SW during its propagation owing to the small compressibility of water. The effect of overheat instabilities and strata formation[19] for wire explosions in water is also significantly smaller than in the case of wire explosions in vacuum or gas because the wire material does not enter the liquid-vapor bi-phase in which thermal instabilities gain fast increment.[20,21] Using underwater electrical explosion of cylindrical Cu wire array, an extreme state of water with pressure up to 0.4 TPa in the vicinity ($\leq$5 μm) of the implosion axis was obtained.[22,23] In the case of underwater electrical explosion of a spherical Cu wire array, the parameters of the "water" in the vicinity (diameter of $\sim$12 μm) of the origin of implosion were estimated as: pressure $\sim$***6*** TPa, temperature $\sim$17 eV, and compression $\sim$8.[24,25] Here, let us note that the parameters of the "water" in the vicinity of the axis or origin of implosion were obtained as the results of one-dimension hydrodynamic simulations coupled with the equation of state (EOS) for Cu and water, and the experimentally measured deposited energy and magnetic pressure. The results of these simulations agree with the measured SW time-of-flight and energy delivered to the water flow and suggest that the cylindrical (spherical) symmetry of the converging SW assumed in the simulations is preserved along the main part of SW convergence.

In this paper, the results of a numerical investigation of the dynamics of azimuthally non-uniform converging SW generated by the underwater explosion of a cylindrical wire array using two-dimensional hydrodynamic simulations are

 © 2013 AIP Publishing LLC

This article is copyrighted as indicated in the abstract. Reuse of AIP content is subject to the terms at: http://scitation.aip.org/termsconditions. Downloaded to IP: 132.68.75.115 On: Wed, 27 Nov 2013 06:53:49

presented. Two different types of azimuthal non-uniformities that can be developed in these experiments have been studied. Non-uniformities of the first type (macro non-uniformities) can be developed relatively far from the converging axis because of slightly different (20%–40%) rates of heating of the wires, resulting in their non-simultaneous explosion. Non-uniformities of the second type (micro non-uniformities) were considered in relatively close proximity to the converging axis ($\sim 200\,\mu$m). These non-uniformities can be associated with, for example, micro-inclusions in water or a small non-uniformity in background temperature at the converging SW front. The results obtained showed that the non-uniformities of the SW that were initially introduced are weakly unstable. Macro non-uniformities are more critical for cumulation of energy since they propagate over a longer distance toward the converging axis, and thus grow stronger. However, for the broad range of experimentally relevant regimes that were considered, non-uniformities remain small, and thus, do not significantly affect the cumulation of energy. It was found that only for macro non-uniformities with a wavelength comparable to the distance from the converging axis does the growth rate become significant and can considerably attenuate the energy cumulation.

II. MODEL DESCRIPTION

An external view of a typical cylindrical wire array used in experiments, as described for example in Ref. 22, is shown in Fig. 1. The wire array is placed between the cathode and anode electrodes inside an experimental chamber filled with water. A converging cylindrical SW in water is produced by the electrical explosion of wires generated by a short ($\leq 10^{-6}$ s) high current (≤ 300 kA) pulse (stored energy ≤ 4 kJ).

The exploding wires and water flow expansion were modeled using mass, momentum, and energy conservation equations for each substance, which can be written in the Lagrangian coordinates in integral form as

$$\frac{d}{dt}\int_{V(t)} \rho dV = 0, \tag{1}$$

$$\frac{d}{dt}\int_{V(t)} \vec{u}\rho dV - \int_{S(t)} (P+Q)\vec{n}dA = 0, \tag{2}$$

$$\frac{d\varepsilon}{dt} - (P+Q)\frac{d}{dt}\left(\frac{1}{\rho}\right) = 0, \tag{3}$$

where $V(t)$ is the control volume and $S(t)$ is its boundary, $\vec{n}$ denotes the outward normal unit vector to this boundary, and ρ, P, and ε are the density, pressure, and internal specific energy density of water, respectively. In a two-dimensional model, the volume integral is replaced by the area integral over the cross-section of the control volume and the surface integral is replaced by the contour integral over the boundary of this cross-section. Artificial viscosity Q was added to the pressure for smoothing the SW front over several numerical cells. For two spatial dimensions, the generalized form of artificial viscosity, developed at Lawrence Livermore Laboratory,[26] was used. Conservation law equations were solved self-consistently together with the EOS database:[27] $P = P(\rho, \varepsilon)$ for each substance. To find numerical solution, Eqs. (1)–(3) were discretized using a cell-centered finite volume method on an unstructured triangular mesh.[28–30] This method was selected because it combines the geometric flexibility of a finite-element method with the simplicity of a finite-difference method. To reduce computational time, the calculation domain was limited to one quarter of a full circle, which implies the $\pi/2$ symmetry assumption. The computational domain that includes water and wires is subdivided into a set of non-overlapping unstructured triangular cells (triangular mesh) in such a way that the wire-water interface lies along corresponding cell boundaries [Fig. 2(a)]. Since in the Lagrangian frame there is no flow through the boundaries of fluid cells, they remain composed of one substance (either water or metal) during the motion, which significantly simplifies the calculation procedure. The triangular mesh was constructed using the Delaunay triangulation algorithm[31] that maximizes the minimum angle of all triangles, and therefore, minimizes their circumcircles (relative to area) and the cumulative error of discretization. Pressure P_c, density ρ_c, and internal energy ε_c are the cell-centered values, while the trajectories $\vec{r}_n$, velocities $\vec{u}_n$, and accelerations $\vec{a}_n$ are determined at the nodes of the mesh. Each triangle is subdivided into quadrilaterals formed by connecting their

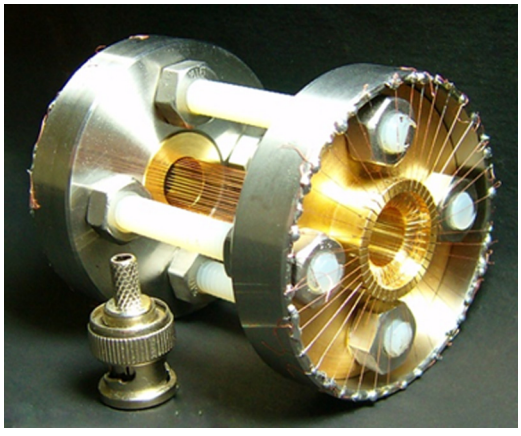

FIG. 1. External view of a cylindrical wire array consisting of 40 Cu wires, each 40 mm in length and 100 μm in diameter.

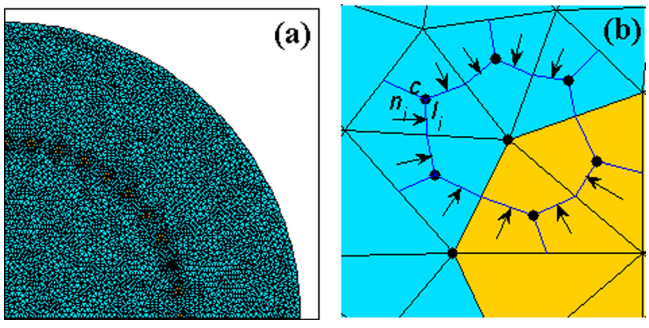

FIG. 2. Discrete staggering (a) Delaunay triangulation. Blue is water. Yellow is metal. (b) Pressure forces acting on polygon surrounding the node. l_i is the length of the "ith" polygon side, $\vec{n}_i$ is the inward normal unit vector to this side, c is centroid of cth cell.

This article is copyrighted as indicated in the abstract. Reuse of AIP content is subject to the terms at: http://scitation.aip.org/termsconditions. Downloaded to IP: 132.68.75.115 On: Wed, 27 Nov 2013 06:53:49

centroids with the midpoints of the opposite sides [Fig. 2(b)]. The acceleration of each node is found from momentum conservation (Eq. (2)) as the net pressure force acting on the surrounding polygon divided by its mass, $\vec{a}_n = \sum_i P_c \vec{n}_i l_i / \sum_c \rho_c (S_c/3)$, where l_i is the length of the "ith" polygon side, $\vec{n}_i$ is the inward normal unit vector to this side, and S_c, ρ_c, and P_c are the area, density, and pressure of the "cth" cell, respectively. Such spatial discretization can be considered as the generalization of the central difference scheme for triangular mesh. An explicit numerical scheme with standard time-centered staggering was used: the velocities were determined at half-integer time steps, while all other values were evaluated at integer time steps. At the first time step, the acceleration $\vec{a}_n^j$ at $t = t^j$ is found from known pressure and density values using the momentum conservation equation. Once the acceleration is known, one can calculate the velocity at $t = t^{j+1/2}$: $\vec{u}_n^{j+1/2}$ and position at $t = t^{j+1}$: $\vec{r}_n^{j+1}$. Now, using the position of each node, the area of each cell and, respectively, the new cell-averaged density ρ_c^{j+1} can be found from the mass conservation equation (Eq. (1)). In linear approximation, cell-averaged values are equal to the cell-centered values (values at the centroids of triangles). Finally, new specific energy ε_c^{j+1} and pressure P_c^{j+1} values are obtained by the iterative solution of the energy conservation equation (Eq. (3)) coupled to EOS. Since such a scheme is explicit, the following Courant-like time step constraint must be used to ensure the stability of the scheme: $\Delta t \leq k \min_C (H_C^{\min}/c_C^{Sound})$, where $H_C^{\min}$ and c_C^{Sound} are the minimum height and sound speed for the "cth" cell, respectively, and the empirical coefficient $k = 1/4$. The propagation of fluids causes significant distortion and tangling of the Lagrangian mesh, which becomes especially severe as the wires expand. The latter results in the loss of accuracy or even complete destruction of the numerical solution. This problem is overcome by a rezoning procedure[32,33] during which a new grid is defined and the Lagrange solution is mapped to the new grid. The values at the nodes of the new grid (accelerations and velocities) are evaluated by linear interpolation between neighboring nodes of the old grid. The cell-averaged density (specific energy) is found as the total mass (total internal energy) of the new triangle divided by its area (total mass): $\rho_{c_N} = \sum_{c_O} \rho_{c_O} S_{c_O c_N} / \sum_{c_O} S_{c_O c_N}$, $\varepsilon_{c_N} = \sum_{c_O} \varepsilon_{c_O} \rho_{c_O} S_{c_O c_N} / \sum_{c_O} \rho_{c_O} S_{c_O c_N}$, where $S_{c_O c_N}$ is the area of overlap between the new triangle c_N and old triangle c_o. The value of pressure is obtained from the density and specific energy using the EOS. The rezoning procedure is applied when a minimum threshold value of triangles quality $q = S_c/(h_1^2 + h_2^2 + h_3^2)$ is achieved, where S_c is the triangle area and h_i are its side lengths. To improve the resolution of the flow features in the proximity of the converging axis without an excessive increase in computational time, an adaptive mesh refinement procedure was applied. Namely, when the front of the SW reaches some radius, each triangle within this radius is divided into four triangles of the same shape. This refinement procedure is invoked several times, and thus, the resolution of the SW is gradually increased as it moves toward to the converging axis. As in the case of the rezoning, the change in the grid must be followed by mapping the Lagrange solution to the new grid, which is accomplished using the procedure described above. In fact, such a mapping procedure is not conservative, which could lead to a significant error in calculations. The error of such a procedure is of second order of cell size, since it utilizes linear interpolation. This error could be significant at the shock wave front where cells become strongly deformed, especially when the shock wave front approaches the converging axis. In the simulations, however, the rezoning procedure was employed at the earlier stage of the SW generation, when the wires are exploding, and later for refinement of the non-disturbed water cells before the converging SW front, when the SW front approaches a half and quarter of the array radius. Therefore, this procedure should not significantly affect the simulation results. The simulation algorithm was developed on MATLAB 2012b platform and carried out on a PC with an Intel(R) core(TM) i7-3770 processor and 32 GB RAM.

III. RESULTS OF MODELING

Below, we present the results of numerical simulations of converging SW generated by the electrical explosion of a cylindrical wire array with a diameter of 5 mm and length of 40 mm made of 40 copper wires, each being 100 μm in diameter. The explosion of the wires was produced by a high-current pulse of ~300 kA maximal amplitude and rise time of ~400 ns emitted by a pulsed generator with stored energy of ~4 kJ. The dependence of the input power on time (Fig. 3 and Table I) was taken from typical UEWE experiments.[22] In the model, skin effect was neglected and homogeneous wire heating was supposed.[34]

The results for macro non-uniformities that were initiated relatively far from the converging axis by unequal power distribution between different wires are shown in Figs. 4(a) and 4(b). Here, one can see a relative mean standard deviation of the SW front radius $\delta R/\bar{R} = \sqrt{\int_0^{2\pi} [R(\varphi) - \bar{R}]^2 d\varphi}/\bar{R}$ with respect to the mean radius of the SW front $\bar{R} = \int_0^{2\pi} R(\varphi) d\varphi$, where the SW front was determined as the isobar line at 50 bar. The plots in Figs. 4(a) and 4(b) correspond to an initial 40% and 20% difference in power distribution between different wires, respectively. Wires with higher (10% or 20% higher than average power) and lower (10% or 20% lower than average power) power input alternate periodically. Here, average power is determined as a power equal to the total power divided by the number of wires. In the case of total number of wires of 40, for dipole-shaped non-uniformity

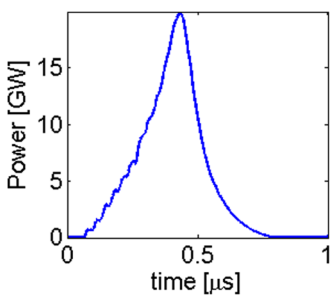

FIG. 3. Power vs. time obtained in underwater electrical explosion of cylindrical wire array of 40 Cu wire array.[22]

This article is copyrighted as indicated in the abstract. Reuse of AIP content is subject to the terms at: http://scitation.aip.org/termsconditions. Downloaded to IP: 132.68.75.115 On: Wed, 27 Nov 2013 06:53:49

TABLE I. Tabulated data of the power deposited to exploding cylindrical array (see Fig. 3).

Time, ns	50	100	150	200	250	300	350	400	450	500	550	600	650
Power, GW	0	0.72	2.93	4.5	6.72	9.4	12.7	17.7	18.5	10.6	5.51	3.16	1.67

(blue dash curves in Fig. 4) each 10 wires with higher power input follow by 10 wires with lower power input. In the case of quadrupole-shaped non-uniformity (red solid curves in Fig. 4), each 5 higher power wires follow by 5 lower power wires. For odd-even non-uniformity (black dash-dot curves in Fig. 4), each higher power wire is alternated by lower power wire. The total power distributed between all 40 wires, as shown in Fig. 3, is identical in all these cases. One can see that only dipole-shaped non-uniformity results in pronounced ($\delta R/\bar{R} \approx 20\%$ and $\delta R/\bar{R} \approx 10\%$ for a 40% and 20% difference in power distribution between different wires, respectively) SW non-uniformity in the vicinity of the implosion axis. The dynamics of the SW non-uniformities can be qualitatively explained by the geometrical Chester-Chisnell-Witham (CCW) model.[10,12] According to this model, the dynamics of the SW can be explained qualitatively by corrugation and convergence effects. The corrugation effect follows from distribution of the pressure at the corrugated front of SW (Fig. 5). Namely, regions with higher curvature experience higher pressure (red arrows) and hence accelerate more strongly. Regions with higher curvature lag behind the mean SW radius and thus this effect tends to cause these regions to catch up with the equilibrium position of the SW front having a mean radius. Once accelerated, these regions can pass this equilibrium position and continue to advance ahead of it, resulting in the oscillations of perturbations around the azimuthally averaged SW front. This effect is more pronounced for perturbations with short wavelengths, i.e., the wavelength is much smaller than the distance to the implosion axis, since these perturbations have stronger variation in curvature. The convergence effect results from the acceleration of the SW due to convergence, i.e., regions of smaller curvature are advanced closer to the axis and, therefore, these regions experience higher pressure and acceleration, which tends to increase the non-uniformity further. A snapshot of the SW for 40% odd-even non-uniformity at $\bar{R} = 0.237$ cm is shown in Fig. 6(a) on the background of pressure distribution. In the vicinity of the exploding wires, one obtains an initially corrugated SW front resulting from the overlapping of individual SWs generated by each wire. In agreement with previously reported results,[35] the originally corrugated SW is self-aligned into a cylindrically symmetric converging front over a very short propagation distance. The fast self-alignment occurs because at this relatively long distance from the axis, the corrugation effect of very short wave-length perturbations greatly exceeds the convergence effect. This explains the almost zero deviation $\delta R/\bar{R} \to 0$ in the rightmost parts in Figs. 4(a) and 4(b). The region of $\delta R/\bar{R} \to 0$ is followed by a region where the perturbations grow. Perturbations having the longest wave-length (dipole-shaped) exhibit the highest, almost steady growth [blue dash curves in Figs. 4(a) and 4(b)] because the corrugation effect for such perturbations is smaller than the convergence effect. A snapshot of such a dipole-shaped SW for 40% non-uniformity is shown in Fig. 6(b) at $\bar{R} = 0.01$ cm. For perturbations of shorter wavelength (quadrupole-shaped), the corrugation effect becomes comparable to the convergence effect, resulting in a weaker growth of the deviation [red solid curves in Figs. 4(a) and 4(b)]. A snapshot of such a quadrupole-shaped SW for 40% non-uniformity is shown in Fig. 6(c) at $\bar{R} = 0.13$cm. Similar behavior with a weak growth and oscillations at the SW front was observed for macro non-uniformity of shortest wave-length (odd-even) shown by black dash-dot curves in Figs. 4(a) and 4(b). A snapshot of the SW front for 40% odd-even non-uniformity at $\bar{R} = 0.034$ cm is shown in Fig. 6(d).

The influence of the different non-uniformities on the maximal pressure behind the SW front in the vicinity ($r \sim 5\,\mu$m) of the implosion axis is shown in Fig. 7(a) (40% difference in power distribution) and Fig. 7(b) (20% difference in

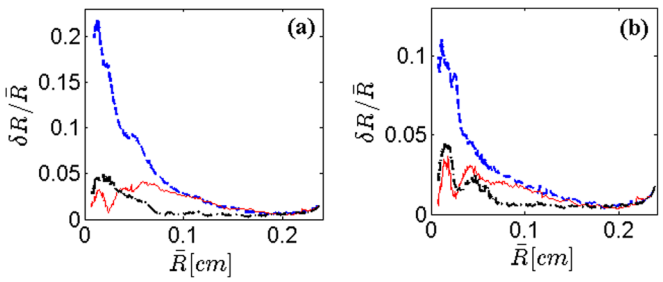

FIG. 4. Dynamics of 40% (a) and 20% (b) macro non-uniformities. Relative mean standard deviation of the SW front radius $\delta R/\bar{R}$ vs. the mean radius $\bar{R}$ for dipole-shaped (blue dash curves), quadrupole-shaped (red solid curves) and odd-even (black dashed-dotted curves) non-uniformities.

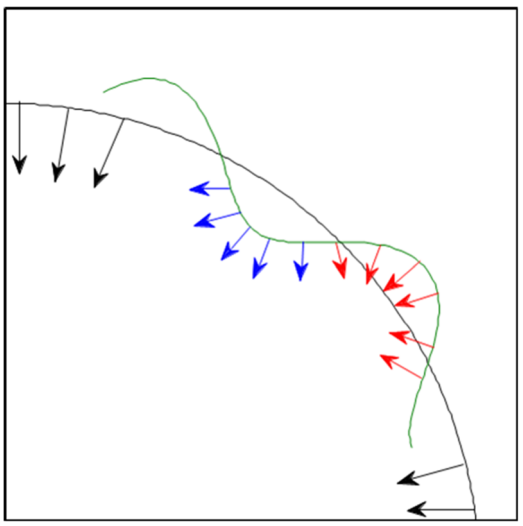

FIG. 5. Scheme showing the corrugation effect: higher curvature regions (red arrows) accelerate stronger then lower curvature region (blue arrows); and convergence effect: regions of smaller curvature are advanced closer to the axis and, therefore, accelerate stronger.

This article is copyrighted as indicated in the abstract. Reuse of AIP content is subject to the terms at: http://scitation.aip.org/termsconditions. Downloaded to IP: 132.68.75.115 On: Wed, 27 Nov 2013 06:53:49

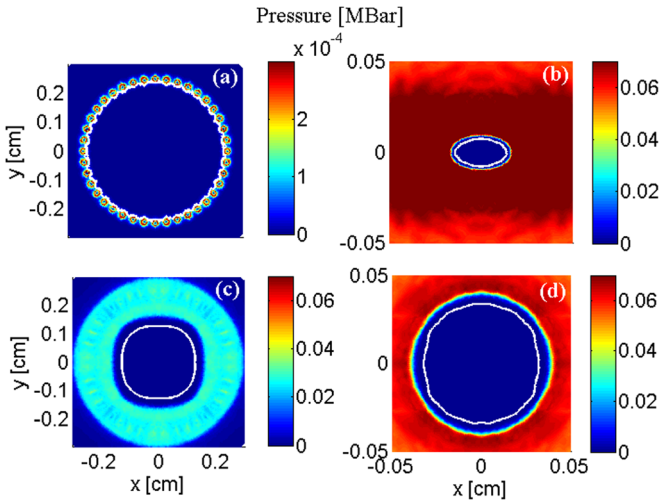

FIG. 6. SW front (isobar at $P = 50$ bar) on background of pressure. (a) Initially corrugated SW formed by overlapping of individual SWs generated by each wire; (b) dipole-shaped SW; (c) quadrupole-shaped SW; (d) SW corrugated by odd-even non-uniformity.

power distribution). This pressure corresponds to the pressure in one of the cells which are adjacent to the axis. In fact, the value of the pressure should be found from the EOS using internal energy and density averaged over two cells adjacent to the axis. The sides of each of these cells are $\sim 5\ \mu$m and, therefore, this value of the pressure corresponds to the pressure averaged over the 5 μm-radius circle around the axis. Nevertheless, the results of additional simulations showed that such averaged pressure is only $\sim$14% different from the pressure in one of the cells in the most unstable case of 40% dipole-shaped non-uniformity. Figs. 7(a) and 7(b) show that the cumulation is significantly (approximately two-fold) reduced only in this most extreme case.

In Figs. 8(a)–8(d), the results of simulations for micro non-uniformities that were initiated at distances of several hundreds of microns from the converging axis are shown. These non-uniformities, which can be associated with, for example, micro-inclusions in water or a small non-uniformity in background temperature, were modeled by artificial energy sources. These sources, being approximately round in shape with radius $\Delta r = 20\mu\text{m} \sim r_c/n$, were centered at the radius $r_c = 200\mu$m with angular periodicity π/n, $n = 8$ [Fig. 8(a)]. The space-time dependence of the energy realized in each source, which results in azimuthally

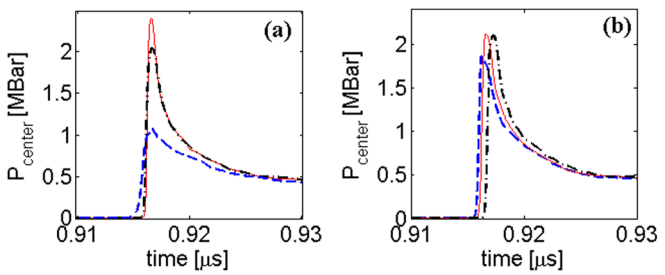

FIG. 7. Pressure distributions in the vicinity of implosion axis ($r \sim 5\ \mu$m) vs. time for 40% (a) and 20% (b) macro non-uniformities in the case of dipole-shaped (blue dashed curves), quadrupole-shaped (red solid curves) and odd-even (black dashed-dotted curves) non-uniformities.

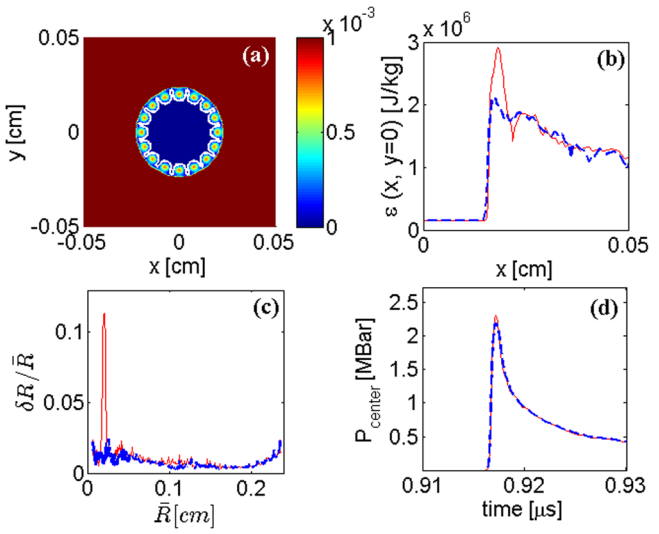

FIG. 8. Effect of micro non-uniformities modeled by artificial energy sources introduced at $r_c = 200\mu$m; (a) initially corrugated SW front (isobar at $P = 50$ bar) on background of pressure; high-pressure spots correspond to artificial energy sources; (b) snapshots of internal energy profiles on $y = 0$ axis with (red solid curve) and without (blue dashed curve) artificial energy sources; (c) relative mean standard deviation of the SW front radius $\delta R/\bar{R}$ vs. the mean radius $\bar{R}$; (d) pressure in the vicinity of implosion axis ($r \sim 5\ \mu$m) vs. time with (red solid curve) and without (blue dashed curve) artificial energy sources.

periodic high-pressure regions, was modeled as: $w = w_0\delta[t - t_c, \tau]\ \exp[-(r - r_c)^2/\Delta r^2]\cos^2(n\varphi)$, $\delta(t, \tau) = \{1 \forall t \in [-\tau, \tau], 0 \forall t \notin [-\tau, \tau]\}$. Here, $w_0 = 4.5 \times 10^7 \text{J}/(\text{kg}\,\mu s)$ is the maximum rate of the energy density deposition at peak time $t_c = 0.88\mu$s and $\tau = 0.008\mu$s is the duration of the energy realized in the sources. This duration was chosen such that the additional pressure would significantly affect only the front of the SW as it passes through $r_c = 200\mu$m and results in a $\sim$40% increment in the internal energy density of water [Fig. 8(b)]. The results of these simulations are shown in Fig. 8(c), where we present the relative mean standard deviations $\delta R/\bar{R}$ of the SW vs. $\bar{R}$ for the cases with micro non-uniformities (red solid curve) and without any non-uniformities, other than those caused by overlapping of individual SWs from each wire (blue dash curve). It can be seen that the SW front significantly ($\delta R/\bar{R} \approx 12\%$) corrugated by micro non-uniformities [shown by the white isobar line at 50 bar in Fig. 8(a)] is self-aligned into a cylindrically symmetric converging front over a very short propagation distance ($\sim$60 μm) because the perturbation wave-length is much shorter than the distance to the converging axis, and therefore, the corrugation effect greatly exceeds the convergence effect. Fig. 8(d) shows the maximal achievable pressure in the vicinity ($r \sim 5\ \mu$m) of the implosion axis vs. time for the cases with (red solid curve) and without (blue dash curve) non-uniformities. One can see that the considered micro non-uniformities almost do not affect the energy cumulation; the peak energy density is slightly higher ($\sim$7%) in the case of micro non-uniformities due to the additional power input by the artificial energy sources. Finally, to verify our numerical results, we ran simulations for the coarser mesh (twice longer mesh edges) and compared the temporal dependences of the pressure at the converging axis for the

This article is copyrighted as indicated in the abstract. Reuse of AIP content is subject to the terms at: http://scitation.aip.org/termsconditions. Downloaded to IP: 132.68.75.115 On: Wed, 27 Nov 2013 06:53:49

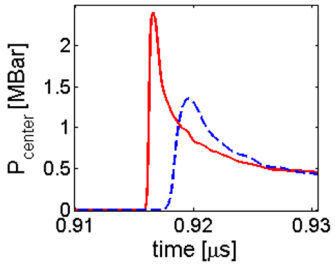

FIG. 9. Pressure in the vicinity of implosion axis vs. time for quadrupole-shaped 40% non-uniformities evaluated on meshes which edges differ by a factor of two in length. Coarser mesh (blue dashed curve) results in ~0.3% shift of implosion time as compared to the finer mesh (red solid curve).

case of quadrupole-shaped 40% macro non-uniformities. The results of the comparison are presented in Fig. 9. One can see that maximum pressure is smaller for the coarser mesh since in finite volume methods the pressure is averaged over the cell and, accordingly, the bigger cell size results in a smaller pressure, which decays fast versus the distance from the axis. However, the times of implosion are only 0.3% (3 ns) different. This implies that the dependence of the SW velocity on the cell size is insignificant.

IV. SUMMARY

In conclusion, using two-dimensional hydrodynamic simulations, we investigated the dynamics and stability of azimuthally non-uniform converging SW generated by the underwater electrical explosion of a cylindrical wire array and the effect of these instabilities on the cumulation of energy in the vicinity of the converging axis. The results were qualitatively explained using the simple geometrical Chester-Chisnell-Witham model. These results show that azimuthal non-uniformities are always weakly unstable; yet, for a broad range of experimentally relevant regimes they remain small and do not significantly affect the cumulation of energy. However, the growth rate of non-uniformities increases with their wave-length and, when the wavelength of non-uniformities becomes comparable to the distance from the converging axis (as for example in the case of dipole-shaped front of SW), they exhibit substantial growth, which considerably attenuates the energy cumulation in the vicinity of converging axis.

ACKNOWLEDGMENTS

The authors are grateful to A. Grinenko, V. Lobatchev, and O. Antonov for fruitful discussions. This research was supported by the Israel Science Foundation Grant No. 99/12.

[1]V. E. Fortov and I. T. Iakubov, *The Physics of Non-Ideal Plasma* (World Scientific, Singapore, 2000).
[2]G. H. Miller, E. I. Moses, and C. R. Wuest, Nucl. Fusion **44**, S228 (2004).
[3]R. J. Leeper, T. E. Alberts, J. R. Asay, P. M. Baca, K. L. Baker, S. P. Breeze, G. A. Chandler, D. L. Cook, G. W. Cooper, C. Deeney *et al.*, Nucl. Fusion **39**, 1283 (1999).
[4]K. Terao, in *Proceedings of 35th Intersociety Energy Conversion Engineering Conference and Exhibit Las Vegas, NV, USA* (2000), vol. 2, p. 915.
[5]A. Grinenko, V. Tz. Gurovich, and Ya. E. Krasik, Phys. Plasmas **14**, 012701 (2007).
[6]S. I. Anisimov, V. E. Bespalov, V. I. Vovchenko, A. N. Dremin, F. I. Dubovitskii, A. P. Zharkov, M. F. Ivanov, I. K. Krasyuk, P. P. Pashinin, A. M. Prokhorov, V. Ya. Ternovoi, V. E. Fortov, and L. N. Shchur, JETP Lett. **31**, 61 (1980).
[7]I. V. Sokolov, Usp. Fiz. Nauk **160**, 143 (1990).
[8]S. P. D'yakov, Zh. Eksp. Teor. Fiz. **27**, 288 (1954).
[9]V. M. Kontorovich, Sov. Phys. JETP **6**, 1179 (1958).
[10]G. B. Whitham, *Linear and Nonlinear Waves* (Wiley, New York, 1974).
[11]L. D. Landau and E. M. Lifshitz, *Fluid Mechanics* (Pergamon, New York, 1987).
[12]J. H. Gardner, D. L. Brook, and I. B. Bernstein, J. Fluid Mech.**114**, 41 (1982).
[13]V. Eliasson, M. Kjellander, and N. Apazidis, Shock Waves **17**, 43 (2007).
[14]D. W. Schwendeman and G. B. Whitham, Proc. R. Soc. London, Ser. A **413**, 297 (1987).
[15]D. W. Schwendeman, J. Fluid Mech. **454**, 365 (2002).
[16]S. Bodner, Phys. Rev. Lett. **33**, 761 (1974).
[17]M. G. Haines, Plasma Phys. Controlled Fusion **53**, 093001 (2011).
[18]A. A. Charakhch'yan, Plasma Phys. Controlled Fusion **39**, 237 (1997).
[19]V. I. Oreshkin, K. V. Khishchenko, P. R. Levashov, A. G. Rousskikh, and S. A. Chaikovskii, High Temp. **50**, 584 (2012).
[20]V. I. Oreshkin, Phys. Plasmas **15**, 092103 (2008).
[21]D. Sheftman and Ya. E. Krasik, Phys. Plasmas **18**, 092704 (2011).
[22]A. Fedotov-Gefen, S. Efimov, L. Gilburd, G. Bazalitski, V. Tz. Gurovich, and Ya. E. Krasik, Phys. Plasmas **18**, 062701 (2011).
[23]L. Gilburd, S. Efimov, A. Fedotov-Gefen, V. Tz. Gurovich, G. Bazalitzky, O. Antonov, and Ya. E. Krasik, Laser Part. Beams **30**, 215 (2012).
[24]O. Antonov, L. Gilburd, S. Efimov, G. Bazalitski, V. Tz. Gurovich, and Ya. E. Krasik, Phys. Plasmas **19**, 102702 (2012).
[25]O. Antonov, S. Efimov, D. Yanuka, M. Kozlov, V. Tz. Gurovich and Ya. E. Krasik, Appl. Phys. Lett. **102**, 124104 (2013).
[26]M. L. Wilkins, J. Comput. Phys. **36**, 281 (1980).
[27]See National Technical Information Service Document No. DE85014241 (S. P. Lyon and J. D. Johnson, Sesame: The Los Alamos National Laboratory Equation-of-State Database, LANL Rep. LA-UR-92-3407, 1992). Copies may be ordered from the National Technical Information Service, Springfield, VA, 22161.
[28]J. C. Campbell and M. J. Shashkov, Selcuk J. Appl. Math. **4**, 53 (2003).
[29]R. Liska, M. Shashkov, and B. Wendroff, *in Proceedings of Mathematical and Computer Modeling in Science and Engineering, International Conference in Honor of the 80th Birthday of K. Rektorys, Prague*, edited by M. Kocandrlova and V. Kelar (2003), p. 216.
[30]S. Sambasivan, M. Shashkov, and D. Burton, Int. J. Numer. Methods Fluids **72**, 770 (2013).
[31]B. Delaunay, Otdelenie Matematicheskih i Estestvennykh Nauk **7**, 793 (1934).
[32]L. G. Margolin, J. Comput. Phys. **135**, 198 (1997).
[33]L. G. Margolin and M. Shashkov, J. Comput. Phys. **184**, 266 (2003).
[34]D. Sheftman, D. Shafer, S. Efimov, and Ya. E. Krasik, Phys. Plasmas **19**, 034501 (2012).
[35]A. Fedotov, A. Grinenko, S. Efimov, and Ya. E. Krasik, Appl. Phys. Lett. **90**, 201502 (2007).

This article is copyrighted as indicated in the abstract. Reuse of AIP content is subject to the terms at: http://scitation.aip.org/termsconditions. Downloaded to IP: 132.68.75.115 On: Wed, 27 Nov 2013 06:53:49